Computers and Mathematics with Applications 66 (2013) 943–964

Contents lists available at ScienceDirect

Computers and Mathematics with Applications

journal homepage: www.elsevier.com/locate/camwa

A viscoelastic model for random ultrasound propagation in cancellous bone

Robert P. Gilbert, Philippe Guyenne *, Jing Li

Department of Mathematical Sciences, University of Delaware, Newark, DE 19716, USA

ARTICLE INFO

Article history:
Received 14 December 2012
Received in revised form 24 June 2013
Accepted 29 June 2013

Keywords:
Cancellous bone
Random waves
Ultrasound
Viscoelastic material

ABSTRACT

In this paper, we perform time-domain simulations of ultrasound interrogations on cancellous bone. We are interested in describing the attenuation of displacement as a function of frequency as well as of bone porosity. A representative volume element for the cancellous bone is constructed using a two-dimensional random distribution of fluid and solid particles, via the *turning bands method*. Our numerical results compare favorably with those obtained from homogenization methods.

1. Introduction

Ultrasound has been considered as a means to characterize the elastic properties of cortical and cancellous bone for some time [1–32].

One experiment involves computing the spectrum of the phase velocity $c(f_c)$ and that of the attenuation rate $\alpha(f_c)$, where f_c is the frequency of the sound wave. Many investigations report that attenuation depends linearly on frequency from 200 to 600 kHz and in the range of 600 kHz to 1 MHz [22,24,33]. We emulate some of these experiments in our computer simulations described below. We observe this increase in attenuation as frequency increases; however, not enough frequencies were computed to suggest a functional relationship for $\alpha(f_c)$.

Prior numerical work on this subject is usually divided into frequency-domain (e.g. [34]) and time-domain models (e.g. [3,4,17,35–38]). In particular, Hosokawa [36] performed three-dimensional simulations but with interrogations in the main trabecular direction. Bossy et al. [35] also considered three-dimensional simulations with quasi-plane waves using a variant of the Graves method [39].

In this paper, we introduce a composite viscoelastic model for ultrasound propagation through cancellous bone in the time domain. We restrict ourselves to the two-dimensional case. In view of applications to quantitative ultrasound techniques for the diagnosis of such bone diseases as osteoporosis, we pay particular attention to bone samples of high porosity. Compared to the mixture approach of Gilbert et al. [40], the present model presents a number of new features:

(i) In view of more realistic simulations, the domain is specified to be a random distribution of points that are either fluid or solid. This is motivated by CT-scans of bone that usually show a very irregular microstructure. The turning bands method is adapted and used to produce two-dimensional isotropic random fields from which random spatial distributions of fluid–solid points can be generated for a given porosity. To our knowledge, this is the first time that the turning bands method is applied to a bone problem.

* Corresponding author. Tel.: +1 3028318664.
E-mail addresses: gilbert@math.udel.edu (R.P. Gilbert), guyenne@math.udel.edu (P. Guyenne), jli@math.udel.edu (J. Li).

0898-1221/$ – see front matter © 2013 Elsevier Ltd. All rights reserved.
http://dx.doi.org/10.1016/j.camwa.2013.06.022

(ii) Both the fluid and solid parts include viscosity to closely account for ultrasound attenuation through cancellous bone, as observed in many laboratory experiments [11,22,30,41,42]. A parametric analysis is conducted to determine physically relevant values for the viscosity coefficients. The resulting equations can be cast into a stress–velocity formulation that lends itself well to discretization by a staggered-grid finite difference method.

In reality, bone tissue is not isotropic and the fluid–solid constituents are not truly randomly distributed. As a consequence, the proposed methods do not apply directly to bone tissues. In the present paper, we explore the possibility to describe bone microstructure by using a flexible and efficient random model. This is motivated in part by previous numerical studies such as [35] which suggest that ultrasound attenuation through cancellous bone is mainly due to scattering by the complex trabecular network.

The remainder of the paper is organized as follows. We introduce the viscoelastic model for ultrasound propagation through cancellous bone in Section 2, and reformulate the equations in terms of the stress and velocity variables in Section 3. We recall the staggered-grid finite difference scheme to discretize these equations in Section 4 and present the turning bands method to generate two-dimensional random fields in Section 5. Finally, we perform a number of numerical simulations to verify the model in Section 6.

2. Viscoelastic model

If we account for dissipation in the solid part of cancellous bone, i.e. the trabeculae, the constitutive equations may be written as

$$\boldsymbol{\tau}^{(s)} = A^{(s)} e(\mathbf{u}) + B^{(s)} e(\mathbf{v}),$$

for the stress tensor, where

$$e(\mathbf{u})_{ij} = \frac{1}{2}\left(\frac{\partial u_i}{\partial x_j} + \frac{\partial\, u_j}{\partial x_i}\right), \qquad e(\mathbf{v})_{ij} = \frac{1}{2}\left(\frac{\partial\, v_i}{\partial x_j} + \frac{\partial\, v_j}{\partial x_i}\right), \tag{2.1}$$

and $\mathbf{u}$ and $\mathbf{v}$ are the displacement and velocity fields, respectively.

These constitutive equations may be written in the generalized form

$$\tau_{ij}^{(s)} = A_{ijkl}^{(s)} e(\mathbf{u})_{kl} + B_{ijkl}^{(s)} e(\mathbf{v})_{kl}, \tag{2.2}$$

where the $A_{ijkl}^{(s)}$ are the elasticity coefficients for the solid and are assumed to have the classical symmetry and positivity properties, i.e.

$$A_{ijkl}^{(s)} e_{ij} e_{kl} \geq 0 \quad \text{and} \quad A_{ijkl}^{(s)} = A_{klij}^{(s)} = A_{jikl}^{(s)} = A_{ijlk}^{(s)},$$

while the $B_{ijkl}^{(s)}$ would correspond to instantaneous viscosity terms and we assume that these are also isotropic. In the isotropic elastic case, we have

$$A_{ijkl}^{(s)} e_{kl} = \left(\lambda^{(1)} \delta_{ij}\delta_{kl} + 2\mu^{(1)} \delta_{ik}\delta_{jl}\right) e_{kl} = \lambda^{(1)} \delta_{ij} e_{kk} + 2\mu^{(1)} e_{ij},$$

where $\{\lambda^{(1)}, \mu^{(1)}\}$ are the Lamé parameters, and

$$B_{ijkl}^{(s)} e_{kl} = \left(\lambda^{(2)} \delta_{ij}\delta_{kl} + 2\mu^{(2)} \delta_{ik}\delta_{jl}\right) e_{kl} = \lambda^{(2)} \delta_{ij} e_{kk} + 2\mu^{(2)} e_{ij}, \tag{2.3}$$

where $\{\lambda^{(2)}, \mu^{(2)}\}$ are the viscosity parameters, or more compactly

$$\boldsymbol{\tau}^{(s)} = \lambda^{(1)} \mathbb{I} e(\mathbf{u}) + 2\mu^{(1)} \boldsymbol{e}(\mathbf{u}) + \lambda^{(2)} \mathbb{I} e(\mathbf{v}) + 2\mu^{(2)} \boldsymbol{e}(\mathbf{v}), \tag{2.4}$$

where e is the dilatation, $\boldsymbol{e}$ is the strain tensor and $\mathbb{I}$ is the identity tensor. A plane-strain situation is considered here. The equations of motion for the solid part are given by

$$\partial_t \mathbf{v} = b^{(s)} \operatorname{div}\left[A^{(s)} e(\mathbf{u}) + B^{(s)} e(\mathbf{v})\right], \tag{2.5}$$

in $\Omega_s \times [0, T]$, where $b^{(s)} = 1/\rho^{(s)}$ and $\rho^{(s)}$ are the solid buoyancy and density respectively. In the case where the material is isotropic, these equations take the form

$$\partial_t \mathbf{v} = b^{(s)} \left[\frac{\partial}{\partial x_j}\left(\lambda^{(1)} \delta_{ij} e_{kk}(\mathbf{u}) + 2\mu^{(1)} e_{ij}(\mathbf{u})\right) + \frac{\partial}{\partial x_j}\left(\lambda^{(2)} \delta_{ij} e_{kk}(\mathbf{v}) + 2\mu^{(2)} e_{ij}(\mathbf{v})\right)\right]. \tag{2.6}$$

In the fluid part $\Omega_f \times [0, T]$, by using the small compressibility approximation, the constitutive equations are also of the form (2.2), namely

$$\boldsymbol{\tau}^{(f)} = A^{(f)} e(\mathbf{u}) + B^{(f)} e(\mathbf{v}),$$

with

$$A^{(f)} = c^2 \rho^{(f)}\, \mathbb{I}, \qquad B^{(f)} = 2\eta \mathbb{I},$$

where c is the speed of sound in the fluid and η is the fluid viscosity.

The equations of motion for this Stokes system read

$$\partial_t \mathbf{v} = b^{(f)} \mathrm{div}\left[c^2 \rho^{(f)} \mathrm{div}(\mathbf{u}\mathbb{I}) + 2\,\eta\, e(\mathbf{v})\right], \tag{2.7}$$

in $\Omega_f \times [0, T]$, where $b^{(f)} = 1/\rho^{(f)}$ and $\rho^{(f)}$ are the fluid buoyancy and density respectively.

In both fluid and solid parts, the system of equations for $\boldsymbol{\tau}$, $\mathbf{v}$ and $\mathbf{u}$ is completed by

$$\partial_t \mathbf{u} = \mathbf{v}. \tag{2.8}$$

Free-surface conditions are imposed at the boundary of the full domain $\Omega_f \cup \Omega_s$ [40]. Continuity of displacements, velocities and forces is assumed at the fluid–solid interface.

3. Graves-like scheme

Since the trabeculae is considered to be viscoelastic and isotropic, this leads to a system of equations similar to that in Graves [39] for seismic waves. Restricting our attention to the two-dimensional case in Cartesian coordinates (x, y), the stresses in the trabeculae may be written as

$$\begin{aligned}
\tau_{xx}^{(s)} &= \left(\lambda^{(1)} + 2\mu^{(1)}\right) \partial_x u_x + \lambda^{(1)} \partial_y u_y + \left(\lambda^{(2)} + 2\mu^{(2)}\right) \partial_x v_x + \lambda^{(2)} \partial_y v_y,\\
\tau_{yy}^{(s)} &= \left(\lambda^{(1)} + 2\mu^{(1)}\right) \partial_y u_y + \lambda^{(1)} \partial_x u_x + \left(\lambda^{(2)} + 2\mu^{(2)}\right) \partial_y v_y + \lambda^{(2)} \partial_x v_x,\\
\tau_{xy}^{(s)} &= \mu^{(1)} \left(\partial_x u_y + \partial_y u_x\right) + \mu^{(2)} \left(\partial_x v_y + \partial_y v_x\right),
\end{aligned} \tag{3.1}$$

and their evolution obeys

$$\begin{aligned}
\partial_t \tau_{xx}^{(s)} &= \left(\lambda^{(1)} + 2\mu^{(1)}\right) \partial_x v_x + \lambda^{(1)} \partial_y v_y + \left(\lambda^{(2)} + 2\mu^{(2)}\right) \partial_x \dot{v}_x + \lambda^{(2)} \partial_y \dot{v}_y,\\
\partial_t \tau_{yy}^{(s)} &= \left(\lambda^{(1)} + 2\mu^{(1)}\right) \partial_y v_y + \lambda^{(1)} \partial_x v_x + \left(\lambda^{(2)} + 2\mu^{(2)}\right) \partial_y \dot{v}_y + \lambda^{(2)} \partial_x \dot{v}_x,\\
\partial_t \tau_{xy}^{(s)} &= \mu^{(1)} \left(\partial_x v_y + \partial_y v_x\right) + \mu^{(2)} \left(\partial_x \dot{v}_y + \partial_y \dot{v}_x\right),
\end{aligned} \tag{3.2}$$

where the dot represents differentiation with respect to t (e.g. $\dot{v}_x = \partial_t v_x$). In (3.2), the acceleration field is given by

$$\begin{aligned}
\partial_t\, v_x &= b^{(s)} \left[\, \partial_x \tau_{xx}^{(s)} + \partial_y \tau_{xy}^{(s)} \right],\\
\partial_t\, v_y &= b^{(s)} \left[\, \partial_x \tau_{xy}^{(s)} + \partial_y \tau_{yy}^{(s)} \right].
\end{aligned} \tag{3.3}$$

In the interstitial fluid, the evolution equations for the stress field are

$$\begin{aligned}
\partial_t \tau_{xx}^{(f)} &= c^2 \rho^{(f)} (\partial_x v_x + \partial_y v_y) + 2\eta \partial_x \dot{v}_x,\\
\partial_t \tau_{yy}^{(f)} &= c^2 \rho^{(f)} (\partial_x v_x + \partial_y v_y) + 2\eta \partial_y \dot{v}_y,\\
\partial_t \tau_{xy}^{(f)} &= \eta \left(\partial_x \dot{v}_y + \partial_y \dot{v}_x\right),
\end{aligned} \tag{3.4}$$

combined with

$$\begin{aligned}
\partial_t\, v_x &= b^{(f)} \left[\, \partial_x \tau_{xx}^{(f)} + \partial_y \tau_{xy}^{(f)} \right],\\
\partial_t\, v_y &= b^{(f)} \left[\, \partial_x \tau_{xy}^{(f)} + \partial_y \tau_{yy}^{(f)} \right].
\end{aligned} \tag{3.5}$$

We note that both the fluid and solid phases are described by a general system of the form

$$\begin{aligned}
\tau_{xx}^{(a)} &= \left(\lambda^{(k)} + 2\mu^{(k)}\right) \partial_x u_x + \lambda^{(k)} \partial_y u_y + \left(\lambda^{(k+1)} + 2\mu^{(k+1)}\right) \partial_x v_x + \lambda^{(k+1)} \partial_y v_y,\\
\tau_{yy}^{(a)} &= \left(\lambda^{(k)} + 2\mu^{(k)}\right) \partial_y u_y + \lambda^{(k)} \partial_x u_x + \left(\lambda^{(k+1)} + 2\mu^{(k+1)}\right) \partial_y v_y + \lambda^{(k+1)} \partial_x v_x,\\
\tau_{xy}^{(a)} &= \mu^{(k)} \left(\partial_x u_y + \partial_y u_x\right) + \mu^{(k+1)} \left(\partial_x v_y + \partial_y v_x\right),
\end{aligned} \tag{3.6}$$

together with the evolution equations

$$\begin{aligned}
\partial_t \tau_{xx}^{(a)} &= \left(\lambda^{(k)} + 2\mu^{(k)}\right) \partial_x v_x + \lambda^{(k)} \partial_y v_y + \left(\lambda^{(k+1)} + 2\mu^{(k+1)}\right) \partial_x \dot{v}_x + \lambda^{(k+1)} \partial_y \dot{v}_y, \\
\partial_t \tau_{yy}^{(a)} &= \left(\lambda^{(k)} + 2\mu^{(k)}\right) \partial_y v_y + \lambda^{(k)} \partial_x v_x + \left(\lambda^{(k+1)} + 2\mu^{(k+1)}\right) \partial_y \dot{v}_y + \lambda^{(k+1)} \partial_x \dot{v}_x, \\
\partial_t \tau_{xy}^{(a)} &= \mu^{(k)} \left(\partial_x v_y + \partial_y v_x\right) + \mu^{(k+1)} \left(\partial_x \dot{v}_y + \partial_y \dot{v}_x\right),
\end{aligned} \tag{3.7}$$

where $(a, k) = \{(s, 1), (f, 3)\}$, $\lambda^{(3)} = c^2 \rho^{(f)}$, $\lambda^{(4)} = 0$, $\mu^{(3)} = 0$ and $\mu^{(4)} = \eta$. The acceleration field also has the same form for both phases,

$$\begin{aligned}
\partial_t\, v_x &= b^{(a)} \left[\, \partial_x \tau_{xx}^{(a)} + \partial_y \tau_{xy}^{(a)} \right], \\
\partial_t\, v_y &= b^{(a)} \left[\, \partial_x \tau_{xy}^{(a)} + \partial_y \tau_{yy}^{(a)} \right].
\end{aligned} \tag{3.8}$$

This is completed by

$$\partial_t\, u_x = v_x, \qquad \partial_t\, u_y = v_y, \tag{3.9}$$

which yields the displacements in both phases as well.

4. Discretized systems

We use a staggered-grid finite difference scheme to discretize the system (3.6)–(3.9) in each phase, where the different components of displacement, velocity and stress are defined at different grid points in the computational domain and the variables are also staggered temporally. In our notation, the subscripts refer to the spatial indices while the superscripts refer to the time index. For example, the expression

$$v_{x\, i+\frac{1}{2}, j}^{\,n+\frac{1}{2}},$$

represents the x-component of the velocity at point $x_{i+1/2} = (i+1/2)\Delta x$, $y_j = j\Delta y$ and at time $t_{n+1/2} = (n+1/2)\Delta t$, where Δx, Δy are the mesh sizes in the two spatial directions and Δt is the time step. To avoid overly cumbersome expressions, D_j denotes the difference operator for the discretization of the partial derivative ∂_j in space. The superscript (a) refers to fluid or solid depending on which phase the grid point is in. We briefly present the discretized equations below and refer the reader to [39,40] for further details.

The discretization of (3.7) reads

$$\begin{aligned}
\tau_{xx\, i,j}^{(a)\, n+1} &= \tau_{xx\, i,j}^{(a)\, n} + \Delta t \left[\left(\lambda^{(k)} + 2\mu^{(k)}\right) D_x v_x + \lambda^{(k)} D_y v_y + \left(\lambda^{(k+1)} + 2\mu^{(k+1)}\right) D_x \dot{v}_x + \lambda^{(k+1)} D_y \dot{v}_y\right]_{i,j}^{n+\frac{1}{2}}, \\
\tau_{yy\, i,j}^{(a)\, n+1} &= \tau_{yy\, i,j}^{(a)\, n} + \Delta t \left[\left(\lambda^{(k)} + 2\mu^{(k)}\right) D_y v_y + \lambda^{(k)} D_x v_x + \left(\lambda^{(k+1)} + 2\mu^{(k+1)}\right) D_y \dot{v}_y + \lambda^{(k+1)} D_x \dot{v}_x\right]_{i,j}^{n+\frac{1}{2}}, \\
\tau_{xy\, i+\frac{1}{2}, j+\frac{1}{2}}^{(a)\, n+1} &= \tau_{xy\, i+\frac{1}{2}, j+\frac{1}{2}}^{(a)\, n} + \Delta t \left[\mu^{(k)} \left(D_x v_y + D_y v_x\right) + \mu^{(k+1)} \left(D_x \dot{v}_y + D_y \dot{v}_x\right)\right]_{i+\frac{1}{2}, j+\frac{1}{2}}^{n+\frac{1}{2}},
\end{aligned} \tag{4.1}$$

and the discretized form of (3.8) is

$$\begin{aligned}
v_{x\, i+\frac{1}{2}, j}^{\,n+\frac{1}{2}} &= v_{x\, i+\frac{1}{2}, j}^{\,n-\frac{1}{2}} + b^{(a)} \Delta t \left[D_x \tau_{xx}^{(a)} + D_y \tau_{xy}^{(a)}\right]_{i+\frac{1}{2}, j}^{n}, \\
v_{y\, i, j+\frac{1}{2}}^{\,n+\frac{1}{2}} &= v_{y\, i, j+\frac{1}{2}}^{\,n-\frac{1}{2}} + b^{(a)} \Delta t \left[D_x \tau_{xy}^{(a)} + D_y \tau_{yy}^{(a)}\right]_{i, j+\frac{1}{2}}^{n}.
\end{aligned} \tag{4.2}$$

In the present formulation, Eqs. (4.1) and (4.2) form a closed system of equations for the stress and velocity fields. Free-surface conditions are imposed at the boundaries of the domain. An auxiliary computation determines the displacements from the velocities at every time step, assuming their respective components are defined at the same grid points but staggered temporally. Using centered finite differences in time, the discretization of (3.9) is given by

$$\begin{aligned}
u_{x\, i+\frac{1}{2}, j}^{n+1} &= u_{x\, i+\frac{1}{2}, j}^{n} + \Delta t\, v_{x\, i+\frac{1}{2}, j}^{\,n+\frac{1}{2}}, \\
u_{y\, i, j+\frac{1}{2}}^{n+1} &= u_{y\, i, j+\frac{1}{2}}^{n} + \Delta t\, v_{y\, i, j+\frac{1}{2}}^{\,n+\frac{1}{2}}.
\end{aligned} \tag{4.3}$$

The overall scheme is (formally) second-order in both space and time. Because this scheme is explicit in time, it is thus conditionally stable. A von Neumann stability analysis providing an upper bound for the time step is performed in Appendix A.

5. Turning bands method

In this paper, we assume the domain is a random distribution of fluid and solid points. For this purpose, we adopt the efficient and accurate 'turning bands' method of Mantoglou and Wilson [43] (see also [44]) to simulate multidimensional stationary random fields with a prescribed covariance structure. Because it is a key component of our numerical model, we review this approach in the present section and explain how we adapt it to our bone problem.

Given a point $\mathbf{x} = (x_1, x_2, \ldots, x_n)$ in $\mathbb{R}^n$, the random function $z(\mathbf{x})$ is called a random field. The mean of $z(\mathbf{x})$ is defined as

$$m(\mathbf{x}) = E[z(\mathbf{x})],$$

where E is the expectation, and the covariance function is defined as

$$C(\mathbf{x}_1, \mathbf{x}_1) = E[(z(\mathbf{x}_1) - m(\mathbf{x}_1))(z(\mathbf{x}_2) - m(\mathbf{x}_2))],$$

for all $\mathbf{x}_1, \mathbf{x}_2 \in \mathbb{R}^n$. Here we focus our attention on second-order stationary random fields which require that:

1. The mean is independent of the position of each point,
$$E[z(\mathbf{x})] = m(\mathbf{x}) = m, \quad \forall \mathbf{x} \in \mathbb{R}^n,$$
2. The covariance function only depends on the difference between two points,
$$C(\mathbf{x}_1, \mathbf{x}_2) = C(\mathbf{x}_1 - \mathbf{x}_2) = C(\mathbf{h}), \quad \forall \mathbf{x}_1, \mathbf{x}_2 \in \mathbb{R}^n,$$

where $\mathbf{h}$ is the difference vector. Furthermore, if the covariance function only depends on the distance between two points, i.e.

$$C(\mathbf{h}) = C(r),$$

where $r = |\mathbf{h}|$, then it is called isotropic. In the turning bands method, instead of generating a high-dimensional field directly, several independent one-dimensional processes (evenly distributed in the higher dimension) are simulated and superimposed. Because we restrict ourselves to two-dimensional numerical experiments in the present case, we will only discuss the generation of two-dimensional second-order stationary isotropic random fields.

Assuming the field to be simulated is second-order stationary and isotropic, its value at each point is normally distributed and has zero mean. The covariance function $C(r)$ of the random field is assumed to be known. Fig. 1 shows a schematic representation of the method. Let D denote this two-dimensional field with grid points in both x- and y-directions. First, choose an arbitrary point as the origin O, generate L lines through O such that the directional vectors $\mathbf{u}_i$ of each line are uniformly distributed over the unit circle, with θ_i being the angle between line i and the positive x-axis. Along each line, we simulate a discrete one-dimensional second-order stationary process with zero mean and covariance $C_1(\xi)$. The relationship between $C_1(\xi)$ and $C(r)$ will be discussed later. More specifically, along each line, we define small intervals with length $\Delta\xi$. If we draw a perpendicular line at the end of each interval, we will see a set of bands, as depicted in Fig. 1, hence the terminology 'turning bands' for this method. The one-dimensional process generates a set of discrete values, with each band having a unique value. Let $\mathbf{x}_N$ denote the position vector of point N in the domain, then the projection of $\mathbf{x}_N$ onto line i is $\xi_{Ni} = \mathbf{x}_N \cdot \mathbf{u}_i$ and the assigned value $z_i(\xi_{Ni})$ depends on which band the projection falls into. For the L lines, we generate independent one-dimensional processes with the same covariance $C_1(\xi)$. For every point N in the domain, there are thus L assigned values $z_i(\xi_{Ni})$ and the final assignment is given by the sum

$$z(\mathbf{x}_N) = \frac{1}{\sqrt{L}} \sum_{i=1}^{L} z_i(\mathbf{x}_N \cdot \mathbf{u}_i). \tag{5.1}$$

Note each line should have a minimum length depending on the domain size so that it can cover the projections of all points in the domain.

Next let us show that the generated field has the desired property. It is clear that the field given by (5.1) has zero mean because each one-dimensional process has zero mean. The question remains as to whether the random field has the imposed covariance structure. By definition of the covariance together with (5.1), we have

$$\begin{aligned} C(\mathbf{x}_1, \mathbf{x}_2) &= E[(z(\mathbf{x}_1) - E[z(\mathbf{x}_1)])(z(\mathbf{x}_2) - E[z(\mathbf{x}_2)])] \\ &= E[z(\mathbf{x}_1) z(\mathbf{x}_2)] \\ &= \frac{1}{L} \sum_{i=1}^{L} \sum_{j=1}^{L} E[z_i(\mathbf{x}_1 \cdot \mathbf{u}_i) z_j(\mathbf{x}_2 \cdot \mathbf{u}_j)] \\ &= \frac{1}{L} \sum_{i=1}^{L} C_1(\mathbf{h} \cdot \mathbf{u}_i), \end{aligned} \tag{5.2}$$

where $\mathbf{h} = \mathbf{x}_1 - \mathbf{x}_2$. In (5.2), we have used the fact that the one-dimensional process is second-order stationary and that all $i \neq j$ terms vanish because the processes on two different lines are independent. Since the directional vectors $\mathbf{u}_i$ are uniformly distributed over the unit circle, C_1 is only a function of r for large L, which implies that the two-dimensional process is stationary and isotropic, and we can write

$$C(\mathbf{x}_1, \mathbf{x}_2) = C_s(\mathbf{h}) = C_s(r) = \frac{1}{L}\sum_{i=1}^{L} C_1(\mathbf{h}\cdot\mathbf{u}_i).$$

Therefore, by the law of large numbers,

$$\begin{aligned} C(r) &= \lim_{L\to\infty}\left[\frac{1}{L}\sum_{i=1}^{L} C_1(\mathbf{h}\cdot\mathbf{u}_i)\right] \\ &= E[C_1(\mathbf{h}\cdot\mathbf{u})] \\ &= \int_c C_1(\mathbf{h}\cdot\mathbf{u}) f(\mathbf{u})\, d\mathbf{u} \\ &= \frac{1}{2\pi}\int_c C_1(\mathbf{h}\cdot\mathbf{u})\, d\mathbf{u}, \end{aligned} \tag{5.3}$$

where c represents the unit circle and $f(\mathbf{u})$ is the probability density function of $\mathbf{u}$ which equals $1/(2\pi)$ in the two-dimensional case. Furthermore, if the origin is taken to be at $\mathbf{x}_1$ and the vector $\mathbf{h}$ points in the vertical direction, then $\xi = \mathbf{h}\cdot\mathbf{u} = r\sin\theta$ as depicted in Fig. 2, and

$$C(r) = \frac{2}{\pi}\int_0^{\pi/2} C_1(r\sin\theta)\, d\theta, \tag{5.4}$$

given that C_1 is an even function. The above integral equation relates the one-dimensional covariance $C_1(\xi)$ to the two-dimensional covariance $C(r)$. Although it is difficult to find an explicit analytical expression in most cases, the one-dimensional process can be easily simulated by a spectral method.

Suppose $S(\boldsymbol{\omega})$ is the spectral density function of the covariance $C(\mathbf{h})$ of a two-dimensional process, where $\boldsymbol{\omega}$ is a vector of frequencies. The Fourier transform relates these two functions in the following way,

$$\begin{aligned} C(\mathbf{h}) &= \int_{\mathbb{R}^2} e^{i\mathbf{h}\cdot\boldsymbol{\omega}} S(\boldsymbol{\omega})\, d\boldsymbol{\omega}, \\ S(\boldsymbol{\omega}) &= \int_{\mathbb{R}^2} e^{-i\mathbf{h}\cdot\boldsymbol{\omega}} C(\mathbf{h})\, d\mathbf{h}. \end{aligned} \tag{5.5}$$

If the field is isotropic, then $S(\boldsymbol{\omega}) = S(\omega)$ where $\omega = |\boldsymbol{\omega}|$, and we can define the radial spectral density function of the two-dimensional isotropic process as

$$f(\omega) = \frac{1}{\sigma^2}\int_{c_\omega} S(\omega) d\omega = \frac{2\pi\omega S(\omega)}{\sigma^2},$$

where c_ω is a circle of radius ω and σ^2 is the variance of the process. Eq. (5.5) becomes

$$\begin{aligned} C(r) &= \sigma^2\int_0^\infty f(\omega) J_0(\omega r)\, d\omega, \\ f(\omega) &= \frac{\omega}{\sigma^2}\int_0^\infty C(r) J_0(\omega r)\, dr, \end{aligned} \tag{5.6}$$

where J_0 is the first-kind Bessel function of order zero. From (5.6), if the covariance $C(r)$ of a two-dimensional isotropic process is known, then we can find the corresponding radial spectral density function.

For the one-dimensional process with covariance $C_1(\xi)$, its spectral density function $S_1(\omega)$ is real, symmetric and positive. Therefore, the Fourier representation of $C_1(\xi)$ is

$$C_1(\xi) = \int_{-\infty}^{\infty} e^{i\omega\xi} S_1(\omega)\, d\omega = 2\int_0^\infty \cos(\omega\xi) S_1(\omega)\, d\omega. \tag{5.7}$$

Substituting (5.7) into (5.4), we obtain

$$\begin{aligned} C(r) &= \frac{4}{\pi}\int_0^\infty S_1(\omega)\left[\int_0^{\pi/2}\cos(\omega r\sin\theta)\, d\theta\right] d\omega \\ &= 2\int_0^\infty S_1(\omega) J_0(\omega r)\, d\omega, \end{aligned}$$

and by the Hankel transform,

$$S_1(\omega) = \frac{\omega}{2}\int_0^\infty C(r)J_0(\omega r)\, rdr. \tag{5.8}$$

Comparing (5.8) and the second equation of (5.6), we find

$$S_1(\omega) = \frac{\sigma^2}{2} f(\omega), \tag{5.9}$$

which implies that the spectral density function of the one-dimensional process can be easily determined if the radial spectral density function of the two-dimensional process is known.

In the present model, each point in the domain is either 'fluid' or 'solid'. Therefore we also need to come up with a procedure to select which values of the generated two-dimensional field correspond to fluid or solid points for the prescribed porosity β. Since the field value at each point is normally distributed, this categorization can be achieved by using the error function

$$\mathrm{erf}(z) = \frac{2}{\sqrt{\pi}}\int_0^z e^{-t^2} dt,$$

which is related to the cumulative density function of a standard normal distribution by

$$\Phi(z) = \frac{1}{2} + \frac{1}{2}\mathrm{erf}\left(\frac{z}{\sqrt{2}}\right). \tag{5.10}$$

Suppose z_0 is the critical point such that the probability

$$\mathbb{P}(-z_0 < z < z_0) = \Phi(z_0) - \Phi(-z_0) = \beta,$$

then z_0 can be found by using (5.10) as

$$z_0 = \sqrt{2}\,\mathrm{erf}^{-1}(\beta).$$

Therefore a point in the domain is fluid if its field value is in $[-z_0, z_0]$, otherwise it is a solid point. By this selection, we can guarantee that a proportion of β points out of the total number is fluid. If the normal probability distribution is not standard, then we can always make it so by a change of variables. Numerical illustrations will be provided in the next section.

6. Numerical experiments

In this section, we perform a number of two-dimensional simulations to verify our numerical model and illustrate key features such as dissipative, elastic and random properties. Typical values for physical parameters in the model are listed in Table 1. The Lamé parameter $\lambda^{(1)}$ for the solid phase is defined by

$$\lambda^{(1)} = \frac{\nu E}{(1+\nu)(1-2\nu)}.$$

Because of the large disparity in orders of magnitude between the various parameters, we find it convenient to non-dimensionalize the equations by using a characteristic length scale $\mathcal{L}$ related to the size of the bone sample and a characteristic time scale $\mathcal{T}$ in the ultrasonic range.

6.1. Comparison with exact solution

Let us consider a purely solid material (all points are solid points). In the one-dimensional case, Eqs. (3.7)–(3.9) for $(a, k) = (s, 1)$ reduce to the damped wave equation

$$\partial_t^2 u_x = \frac{\lambda^{(1)} + 2\mu^{(1)}}{\rho^{(s)}}\partial_x^2 u_x + \frac{\lambda^{(2)} + 2\mu^{(2)}}{\rho^{(s)}}\partial_{xxt} u_x, \tag{6.1}$$

for the displacement u_x, with reflecting boundary condition $\partial_x u_x = 0$ at both endpoints $x = 0$ and $x = L_x$. The corresponding stress and velocity are determined by

$$\tau_{xx} = (\lambda^{(1)} + 2\mu^{(1)})\partial_x u_x + (\lambda^{(2)} + 2\mu^{(2)})\partial_x v_x, \quad v_x = \partial_t u_x.$$

Given initial conditions

$$u_x = f(x), \qquad \partial_t u_x = 0,$$

Table 1
Values of physical parameters for cancellous bone as given in [7,17,34].

Parameter	Symbol	Value
Solid bulk modulus	$K^{(s)}$	2.04×10^{10} Pa
Solid shear modulus	$\mu^{(1)}$	0.833×10^{10} Pa
Solid Young's modulus	E	2.2×10^{10} Pa
Poisson's ratio	ν	0.32
Fluid bulk modulus	$K^{(f)}$	2×10^{9} Pa
Frame material density	$\rho^{(s)}$	1960 kg m^{-3}
Pore fluid density	$\rho^{(f)}$	950 kg m^{-3}

the exact solution can be expressed in terms of a Fourier cosine series,

$$u_x(x,t) = a_0 + \sum_{n=1}^{\infty}\left[a_n e^{-\left(C_n-\sqrt{C_n^2-4D_n}\right)t/2} + b_n e^{-\left(C_n+\sqrt{C_n^2-4D_n}\right)t/2}\right]\cos\left(\frac{n\pi x}{L_x}\right). \tag{6.2}$$

Details on the derivation of (6.2) and on the expressions of the Fourier coefficients are given in Appendix B. Following [6], the viscosity coefficients are taken as

$$\lambda^{(2)} = \frac{\delta}{\pi}\lambda^{(1)}, \qquad \mu^{(2)} = \frac{\delta}{\pi}\mu^{(1)}, \tag{6.3}$$

using the logarithmic decrement $\delta = 0.01$ s. To compare with this exact solution, we perform numerical simulations of (3.7)–(3.9) using initial conditions

$$u_x(x,y,0) = f(x) = 0.01\, e^{-100(x-L_x/2)^2}, \qquad v_x(x,y,0) = 0,$$

and

$$\tau_{xx}(x,y,0) = (\lambda^{(1)} + 2\mu^{(1)})f'(x) = -(\lambda^{(1)} + 2\mu^{(1)})(2x - L_x)\, e^{-100(x-L_x/2)^2},$$

which are invariant in the y-direction. The computational domain is a square with side lengths $L_x = L_y = 3$.

Fig. 3 plots the relative L^∞ and L^2 errors between the exact and numerical solutions at $t = 0.5$, for different values of N_x with a fixed $\Delta t = 10^{-4}$. A number of 50 terms is used in the series (6.2) for the exact solution. Given the smoothness of the solution being considered, this number of terms is more than sufficient for the series solution to be reliable. The good agreement (on all three variables u_x, v_x, τ_{xx}) with the -2 slope confirms the second-order accuracy in space of our numerical scheme.

Figs. 4–6 show the comparison between exact and numerical profiles of u_x, v_x and τ_{xx} in the cross-section $y = L_y/2$ at various times. The spatial resolution is $N_x \times N_y = 100 \times 100$ and the time step is $\Delta t = 5 \times 10^{-4}$, where N_x and N_y denote the number of grid points in the x- and y-directions respectively. This simulation reproduces well the splitting of the initial condition into left- and right-moving components, as well as their propagation to and bouncing off the boundaries of the domain. It also shows the damping of the solution with time. For all three variables, the shape of the profile, the propagation speed, the damping and the reflecting boundary condition, as well as the (anti)symmetry of the solution with respect to $x = L_x/2$, are well reproduced numerically. A better agreement can be obtained by increasing the spatial resolution.

6.2. Random domain generation

The random distribution of fluid and solid points in the domain is specified by the turning bands method described previously. For a covariance $C_1(\xi)$ and spectral density $S_1(\omega)$ as given by (5.9), the one-dimensional second-order stationary process can be generated by

$$z_i(\xi_n) = 2\sum_{k=1}^{M}[S_1(\omega_k)\Delta\omega]^{1/2}\cos(\omega_k'\xi_n + \phi_k), \tag{6.4}$$

where $\omega_k = (k - 1/2)\Omega$, $\omega_k' = \omega_k + \delta_\omega$, Ω is the maximum frequency so that the spectral density function $S_1(\omega)$ is well supported within $[0, \Omega]$, $\Delta\omega = \Omega/M$, and M is the number of harmonics chosen large enough to ensure a fine resolution $\Delta\omega$ [45]. The phase shift ϕ_k is taken to be a random variable distributed uniformly on $[0, 2\pi]$. The small perturbation δ_ω is introduced to avoid periodicity. Ideally, as $\Omega \to \infty$, $M \to \infty$ and $\Delta\omega \to 0$, the process given by (6.4) should have zero mean and the desired covariance $C_1(\xi)$.

After generating the L independent one-dimensional processes, we use (5.1) to assemble the two-dimensional field. The number L of lines is another factor which may cause inaccuracy. Fig. 7 shows a comparison between the simulated two-dimensional covariance and the theoretical one for various values of L. The covariance being simulated is a simple

exponential function $C(r) = \sigma^2 e^{-r}$ with $\sigma^2 = 1$. By integrating $C(r)$ through (5.6), it can be shown that the corresponding radial spectral density function is

$$f(\omega) = \frac{\omega}{(1+\omega^2)^{3/2}},$$

as given in [43]. The spectral density function $S_1(\omega)$ required in (6.4) is then determined from $f(\omega)$ by virtue of (5.9).

We use $\Omega = 50$ and $M = 500$ for the one-dimensional process. We observe a fast convergence as L increases, with $L = 16$ yielding an excellent agreement (at least to graphical accuracy). Fig. 8 depicts a realization of the two-dimensional random field $z(\mathbf{x})$ corresponding to this covariance structure. The domain is a 1×1 cm^2 square. Since each point in the field obeys a standard normal distribution, most values fall within the range of standard deviation $[-3, 3]$. Based on the field realization of Fig. 8, we show examples of random spatial distributions of fluid–solid points for $\beta = 0.6, 0.7, 0.8, 0.9$ in Fig. 9, using the categorization described in Section 5. As expected, the proportion of fluid points increases with β. More specifically, patches of solid points shrink as β is increased, which is consistent with the disappearance of the trabecular matrix in the osteoporosis process.

6.3. Calculation of elastic coefficients and effective material parameters

To ensure that the random field effectively represents the composite material that we want to simulate, we now examine the elastic coefficients and material parameters in a plane-strain situation. In Voigt notation,

$$\boldsymbol{\tau} = \begin{bmatrix} \tau_{xx} \\ \tau_{yy} \\ \tau_{xy} \end{bmatrix} = \begin{bmatrix} \tau_1 \\ \tau_2 \\ \tau_6 \end{bmatrix}, \qquad \boldsymbol{e} = \begin{bmatrix} e_{xx} \\ e_{yy} \\ e_{xy} \end{bmatrix} = \begin{bmatrix} e_1 \\ e_2 \\ e_6 \end{bmatrix}.$$

The elasticity (or stiffness) tensor $\mathbf{C}$ can be expressed as

$$\mathbf{C} = \begin{bmatrix} C_{11} & C_{12} & C_{16} \\ C_{21} & C_{22} & C_{26} \\ C_{61} & C_{62} & C_{66} \end{bmatrix}, \tag{6.5}$$

and the relation between stress and strain is

$$\boldsymbol{\tau} = \mathbf{C} \cdot \boldsymbol{e}. \tag{6.6}$$

Therefore, the elasticity tensor can be calculated as the first derivative of the stress tensor with respect to the strain tensor,

$$\mathbf{C} = \frac{\partial \boldsymbol{\tau}}{\partial \boldsymbol{e}}, \tag{6.7}$$

which can be translated numerically to

$$C_{ij} = \frac{\tau_i(\boldsymbol{e}^{p_j}) - \tau_i(\boldsymbol{e})}{p}, \tag{6.8}$$

where $\boldsymbol{e}^{p_j}$ is the perturbed strain tensor such that $e_i^{p_j} = e_i$ for $i \neq j$, $e_i^{p_j} = e_i + p$ for $i = j$, and p is a small perturbation.

The simulation domain is considered here to be a thin slice cut from a long bone and assuming isotropy, the elasticity tensor $\mathbf{C}$ reduces to

$$\mathbf{C} = \begin{bmatrix} C_{11} & C_{12} & 0 \\ C_{12} & C_{11} & 0 \\ 0 & 0 & C_{66} \end{bmatrix},$$

with only three parameters measuring deformations in the (x, y)-plane. To calculate these elastic coefficients, we perturb the strain tensor as indicated in (6.8) and use (3.6) to evaluate the corresponding stress at each point. We then spatially average over the whole domain, for a given random field and porosity, and also average over 10 realizations of the random field for a given porosity. Fig. 10 plots the variation of C_{11} and C_{12} with increasing porosity. These coefficients are measures of the material stiffness and, as expected, their values decrease as β increases (i.e. as the material becomes more porous). In the limit $\beta \to 1$ (purely fluid case), both coefficients tend to 2000 N/mm^2.

Effective material parameters are another point of interest. They are given by the compliance matrix which is the inverse of the elasticity matrix. In the present plane-strain case, the compliance tensor reads

$$\mathbf{S} = \frac{1+\nu}{E} \begin{bmatrix} 1-\nu & -\nu & 0 \\ -\nu & 1-\nu & 0 \\ 0 & 0 & 1 \end{bmatrix} = \mathbf{C}^{-1}.$$

Therefore, once the elasticity coefficients are known, Young's modulus E and Poisson's ratio ν of the composite material can be determined by inverting $\mathbf{C}$. The shear modulus is then obtained from

$$G = \frac{E}{2(1+\nu)}.$$

Table 2
Attenuation coefficients at $f_c = 1$ MHz and corresponding viscosity coefficients for the solid phase. *Source:* α_L is taken from [48], α_T is taken from [49], η_{11} and η_{66} are evaluated from (6.9) and (6.10) while η_{12} is calculated from (6.11).

α_L (dB cm^{-1})	α_T (dB cm^{-1})	η_{11} (Pa s)	η_{12} (Pa s)	η_{66} (Pa s)
4.2	4	267	197	35

Fig. 11 plots the variation of these effective parameters as a function of porosity. We see that both E and G decrease linearly as β increases, while ν shows an opposite tendency. Figs. 10 and 11 also compare our results with those found by Ilic et al. [34] using a homogenized model for ultrasound propagation through cancellous bone. These authors performed numerical simulations with a similar pressure source and similar rectangular bone samples. Our values are overall higher than theirs but they remain comparable and show a similar trend as β varies. Moreover, in the limit $\beta \to 0$, our curve of E consistently tends to the value 2.2×10^{10} Pa used for the solid phase (see Table 1).

6.4. Ultrasound attenuation test

It is well known that ultrasound propagation through cancellous bone experiences attenuation [34,41,42]. This attenuation is more pronounced at higher frequencies and also increases with bone volume fraction (i.e. bone density). In this section, we check numerically that these features of ultrasound attenuation are reproduced well in the present model. For the purpose of this experiment, we choose physically relevant values for the viscosity coefficients, $(\lambda^{(2)}, \mu^{(2)})$ in the solid phase and η in the fluid phase, following [46,47].

For the solid phase, let α_L and α_T be the attenuation rates associated with the longitudinal and transverse modes, respectively. A relation between attenuation rate and viscosity coefficient for the longitudinal mode is given by

$$\alpha_L = \frac{\eta_{11}\omega^2}{2c_L(\lambda^{(1)} + 2\mu^{(1)})}, \tag{6.9}$$

provided $\omega \gg \alpha_L c_L$, where $c_L = \sqrt{(\lambda^{(1)} + 2\mu^{(1)})/\rho^{(s)}}$ is the speed of sound in the longitudinal direction. A similar relation for the transverse mode can be written as

$$\alpha_T = \frac{\eta_{66}\omega^2}{2c_T\mu^{(1)}}, \tag{6.10}$$

provided $\omega \gg \alpha_T c_T$, where $c_T = \sqrt{\mu^{(1)}/\rho^{(s)}}$ is the speed of sound in the transverse direction. Using parameter values listed in Table 1 together with values of α_L and α_T reported in [48,49], we find $\alpha_L c_L = 1.68 \times 10^5$ s^{-1} and $\alpha_T c_T = 8.25 \times 10^4$ s^{-1} while $\omega = 6.3 \times 10^6$ s^{-1} for a characteristic ultrasonic frequency $f_c = 1$ MHz, so the conditions for (6.9) and (6.10) are met here. From (6.9) to (6.10) and the fact that

$$\eta_{12} = \eta_{11} - 2\eta_{66}, \tag{6.11}$$

in the isotropic case, we can evaluate the viscosity coefficients η_{12}, η_{11}, η_{66} (see Table 2) and, accordingly,

$$\lambda^{(2)} = \eta_{12}, \qquad \mu^{(2)} = \eta_{66}.$$

Similarly, for the fluid phase, a relation between attenuation rate and viscosity coefficient reads

$$\alpha_f = \frac{\eta\omega^2}{2cK^{(f)}}, \tag{6.12}$$

provided $\omega \gg \alpha_f c$, where $c = \sqrt{K^{(f)}/\rho^{(f)}}$ and $K^{(f)}$ is the fluid bulk modulus. Again, using parameter values from Table 1 and α_f from [50], we can check that $\alpha_f c = 1.45 \times 10^4$ s^{-1} $\ll \omega$ for a frequency $f_c = 1$ MHz. Recall that $\lambda^{(3)} = c^2\rho^{(f)}$, $\lambda^{(4)} = 0$, $\mu^{(3)} = 0$ and $\mu^{(4)} = \eta$ for the fluid phase. Table 3 lists the value of η obtained from (6.12), which is close to the value $\eta = 1.5$ Pa s used in [17].

Following [34], the bone sample is assumed to be rectangular, 15 mm long in the x-direction and 30 mm wide in the y-direction. The incoming wave is generated by a localized pressure source, centrally located on the left side of the domain ($x = 0$) and defined by

$$\tau_{xx}(0, y, t) = -P\cos(2\pi f_c t)e^{-15(y-L_y/2)^2},$$

where f_c denotes the prescribed temporal frequency, and the mollifier

$$e^{-15(y-L_y/2)^2},$$

Table 3
Attenuation coefficient at $f_c = 1$ MHz and corresponding viscosity coefficient for the fluid phase.
Source: α_f is taken from [50] and η is evaluated from (6.12).

α_f (dB cm^{-1})	c (m s^{-1})	η (Pa s)
1	1451	1.46

is used to avoid discontinuities which may lead to spurious waves propagating in the y-direction. The pressure is applied over a length of about 10 mm on the left side of the bone sample. Its amplitude is set to be $P = 8$ kPa and the choice of porosity will determine the random distribution of fluid–solid points. The spatial resolution $N_x \times N_y = 500 \times 500$ and time step $\Delta t = 10^{-4}$ are selected sufficiently fine so they can resolve well the excitation wavelength and period. Since we expect the excitation to be primarily longitudinal, propagating from left to right in the x-direction, we focus our attention on u_x. For clarity, the dimensionless values in all the following figures are magnified by a factor of 10^3. Therefore, given $\mathcal{L} = 0.01$ m and $\mathcal{T} = 10^{-5}$ s as used in our non-dimensionalization, the actual values of u_x are of order of 10^{-10} m, which is consistent with previous results [34,40]. The transverse displacement u_y (not shown here) is typically of an order of magnitude smaller than u_x.

We first examine ultrasound attenuation caused by the randomness. The random inhomogeneities in the domain are expected to promote scattering of the incoming signal [29,30]. For this purpose, all the viscosity coefficients (in both fluid and solid phases) are set to zero. Fig. 12b shows a two-dimensional color plot of u_x at $t = 1$ for a fixed frequency $f_c = 1.1$ MHz but three different porosities $\beta = 0.72, 0.82, 0.92$. The corresponding distributions of fluid–solid points are depicted in Fig. 12a. For $\beta = 0.72$, the incoming wave is so strongly scattered and attenuated that it barely leaves the close neighborhood of the source. As β increases (i.e. as bone density decreases), the material becomes more fluid and homogeneous. Therefore, the wave tends to be more focused in the longitudinal direction and is able to reach the right side of the domain without much attenuation.

Due to random inhomogeneity, wave attenuation also depends on frequency. Keeping the viscosities 'turned off', Fig. 13 shows u_x at $t = 1$ for a fixed porosity $\beta = 0.82$ but four different frequencies $f_c = 0.9, 1.1, 1.4, 1.7$ MHz. As expected, the higher the excitation frequency, the stronger the wave attenuation. This is because higher-frequency waves have smaller wavelengths and thus are more subject to scattering by the random array of solid patches.

We now include viscosity in both phases (as given by Tables 2 and 3) and repeat the two previous experiments, to investigate the viscous effects (in addition to randomness) on ultrasound propagation. We can see in Figs. 14 and 15 that the amplitude of u_x is further damped by viscosity, in comparison with Figs. 12 and 13. However, these viscous effects are relatively weak and the random patterns with viscosity are overall similar to those without viscosity. For $\beta = 0.82$ and $f_c = 1.7$ MHz, the excitation is so strongly scattered and damped that it is barely noticeable.

7. Conclusions

We have introduced a composite viscoelastic model for ultrasound propagation through cancellous bone, in which the domain is a random distribution of points that are either fluid or solid. To accomplish this, we have adapted and used the turning bands method to produce two-dimensional random fields from which random spatial distributions of fluid–solid points can be generated given a porosity. The resulting equations expressed in the stress–velocity formulation were solved numerically by a second-order staggered-grid finite difference method.

We have performed a number of two-dimensional plane-strain simulations in the time domain to verify the numerical model and illustrate key features such as dissipative, elastic and random properties. In particular, we have examined the dependence of effective parameters of this composite material (e.g. the shear modulus, Young's modulus and Poisson's ratio) on porosity. Our results show that ultrasound is attenuated by viscosity but even more so by the random inhomogeneity of the domain, which promotes scattering. The lower the porosity or the higher the excitation frequency, the stronger the wave attenuation.

Acknowledgments

This research was partially supported by the NSF through grant No. DMS-0920850 and the Simons Foundation through grant No. 246170. P. Guyenne would also like to thank the Institute for Advanced Study (Princeton, NJ) for its hospitality during the academic year 2011–2012.

Appendix A. von Neumann stability analysis

Through a von Neumann stability analysis, we derive a condition on Δt that ensures stability of the numerical scheme. We restrict the analysis to the two-dimensional case as in our numerical simulations. Assuming a displacement field of the

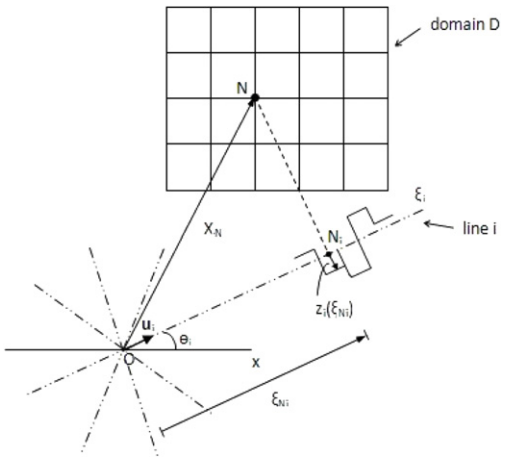

Fig. 1. Schematic representation of the turning bands method.

form

$$\mathbf{u}(\mathbf{x}, t) = (\widehat{u}_x, \widehat{u}_y) e^{i(\mathbf{k}\cdot\mathbf{x}-\omega t)}, \tag{A.1}$$

and substituting $\mathbf{v} = \partial_t \mathbf{u}$ together with (3.6) into the general system (3.8), yield a closed system of equations for the displacement field. The corresponding discretized equations, set up in matrix form, read

$$\begin{bmatrix} (\alpha_k^2 D_{xx} + \beta_k^2 D_{yy}) + \alpha_{k+1}^2 D_{xxt} + \beta_{k+1}^2 D_{yyt} - D_{tt} & (\alpha_k^2 - \beta_k^2) D_{xy} + (\alpha_{k+1}^2 - \beta_{k+1}^2) D_{xyt} \\ (\alpha_k^2 - \beta_k^2) D_{xy} + (\alpha_{k+1}^2 - \beta_{k+1}^2) D_{xyt} & (\alpha_k^2 D_{yy} + \beta_k^2 D_{xx}) + \alpha_{k+1}^2 D_{yyt} + \beta_{k+1}^2 D_{xxt} - D_{tt} \end{bmatrix} \mathbf{u} = \mathbf{0},$$

where

$$\alpha_k = \sqrt{\frac{\lambda^{(k)} + 2\mu^{(k)}}{\rho^{(a)}}}, \qquad \beta_k = \sqrt{\frac{\mu^{(k)}}{\rho^{(a)}}},$$

and

$$\alpha_{k+1} = \sqrt{\frac{\lambda^{(k+1)} + 2\mu^{(k+1)}}{\rho^{(a)}}}, \qquad \beta_{k+1} = \sqrt{\frac{\mu^{(k+1)}}{\rho^{(a)}}},$$

given that $(a, k) = \{(s, 1), (f, 3)\}$ for solid and fluid points, respectively.

This linear system admits a non-trivial solution if and only if the determinant of the coefficient matrix is zero, which implies

$$D_{tt} = \frac{1}{2}\left[\alpha_k^2 + \beta_k^2 - i\omega(\alpha_{k+1}^2 + \beta_{k+1}^2)\right](D_{xx} + D_{yy}) \pm \frac{1}{2}\left[\alpha_k^2 - \beta_k^2 - i\omega(\alpha_{k+1}^2 - \beta_{k+1}^2)\right]\sqrt{(D_{xx} - D_{yy})^2 + 4D_{xy}^2},$$

and hence

$$\sin^2\frac{\omega\Delta t}{2} = \frac{1}{2}\left(\frac{\Delta t}{h}\right)^2 \left| \left[\alpha_k^2 + \beta_k^2 - i\omega(\alpha_{k+1}^2 + \beta_{k+1}^2)\right] \pm \left[\alpha_k^2 - \beta_k^2 - i\omega(\alpha_{k+1}^2 - \beta_{k+1}^2)\right] \right| \left(\sin^2\frac{k_x h}{2} + \sin^2\frac{k_y h}{2}\right), \tag{A.2}$$

after substituting (A.1), where $\mathbf{k} = (k_x, k_y)$ and, for simplicity, we assume that $\Delta x = \Delta y = h$. Details on the difference operators can be found in [39,40]. By requiring that the right-hand side of (A.2) be less than or equal to 1, we arrive at the stability condition

$$\Delta t \le \min\left\{ \frac{h}{\sqrt{2(\alpha_k^4 + \omega^2\alpha_{k+1}^4)^{1/2}}}, \frac{h}{\sqrt{2(\beta_k^4 + \omega^2\beta_{k+1}^4)^{1/2}}} \right\}. \tag{A.3}$$

Note that (α_k, α_{k+1}) represent speeds of longitudinal (or compressional) waves while (β_k, β_{k+1}) represent speeds of transverse (or shear) waves. Since longitudinal waves usually travel faster than transverse waves, i.e. $\alpha_k > \beta_k$ and

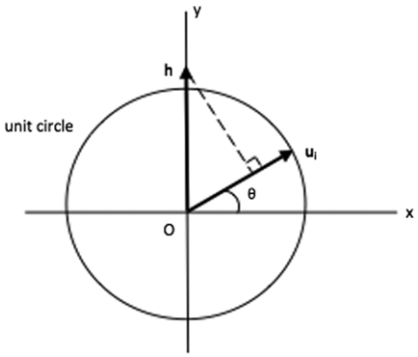

Fig. 2. Definition sketch for the two-dimensional coordinate system with the unit circle as used in the turning bands method.

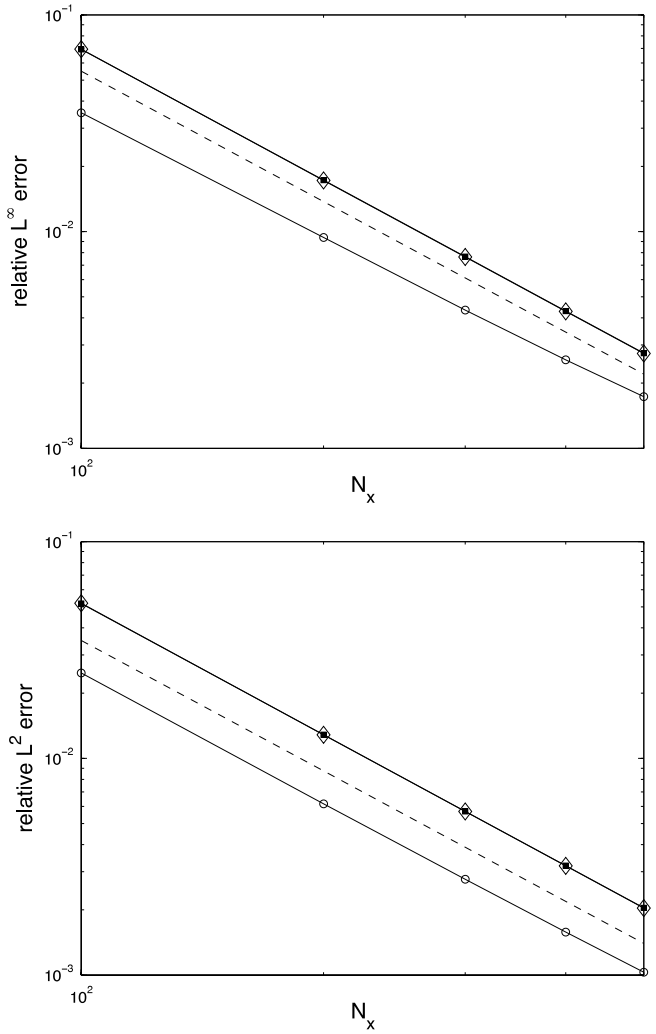

Fig. 3. Relative L^∞ and L^2 errors vs. N_x between the exact and numerical solutions at $t = 0.5$. The displacement u_x is represented in circles, the velocity v_x in diamonds and the stress τ_{xx} in squares. For reference, the dashed line represents the curve N_x^{-2} which has a -2 slope in log–log plot.

$\alpha_{k+1} > \beta_{k+1}$, therefore (A.3) simplifies to

$$\Delta t \leq \frac{h}{\sqrt{2(\alpha_k^4 + \omega^2 \alpha_{k+1}^4)^{1/2}}},$$

which generalizes the stability condition derived in [40] to a viscoelastic material.

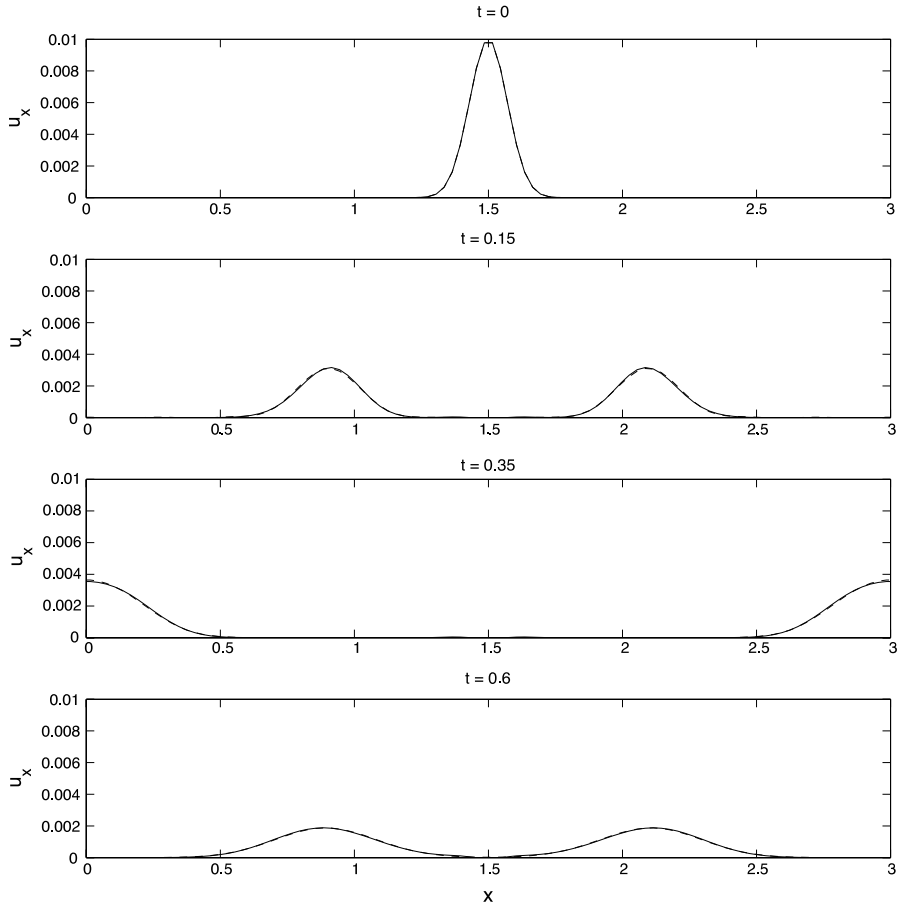

Fig. 4. Profile of displacement u_x in the cross-section $y = L_y/2$ at $t = 0, 0.15, 0.35, 0.6$. The solid line corresponds to the numerical solution while the dashed line corresponds to the exact solution.

Appendix B. Exact solution of the damped wave equation

Consider the damped wave equation

$$\partial_t^2 u_x = \frac{\lambda^{(1)} + 2\mu^{(1)}}{\rho^{(s)}} \partial_x^2 u_x + \frac{\lambda^{(2)} + 2\mu^{(2)}}{\rho^{(s)}} \partial_{xxt} u_x, \tag{B.1}$$

with reflecting boundary conditions

$$\partial_x u_x(0, t) = 0, \qquad \partial_x u_x(L_x, t) = 0, \tag{B.2}$$

and initial conditions

$$u_x(x, 0) = f(x), \qquad \partial_t u_x(x, 0) = 0. \tag{B.3}$$

The corresponding stress and velocity are determined by

$$\tau_{xx} = (\lambda^{(1)} + 2\mu^{(1)})\partial_x u_x + (\lambda^{(2)} + 2\mu^{(2)})\partial_x v_x, \quad v_x = \partial_t u_x.$$

This problem can be solved analytically by separation of variables. Let $u_x(x, t) = X(x)T(t)$, then (B.1) becomes

$$\frac{X}{X''} = \frac{\lambda^{(1)} + 2\mu^{(1)}}{\rho^{(s)}} \left(\frac{T}{T''}\right) + \frac{\lambda^{(2)} + 2\mu^{(2)}}{\rho^{(s)}} \left(\frac{T'}{T''}\right) = -\frac{1}{\kappa},$$

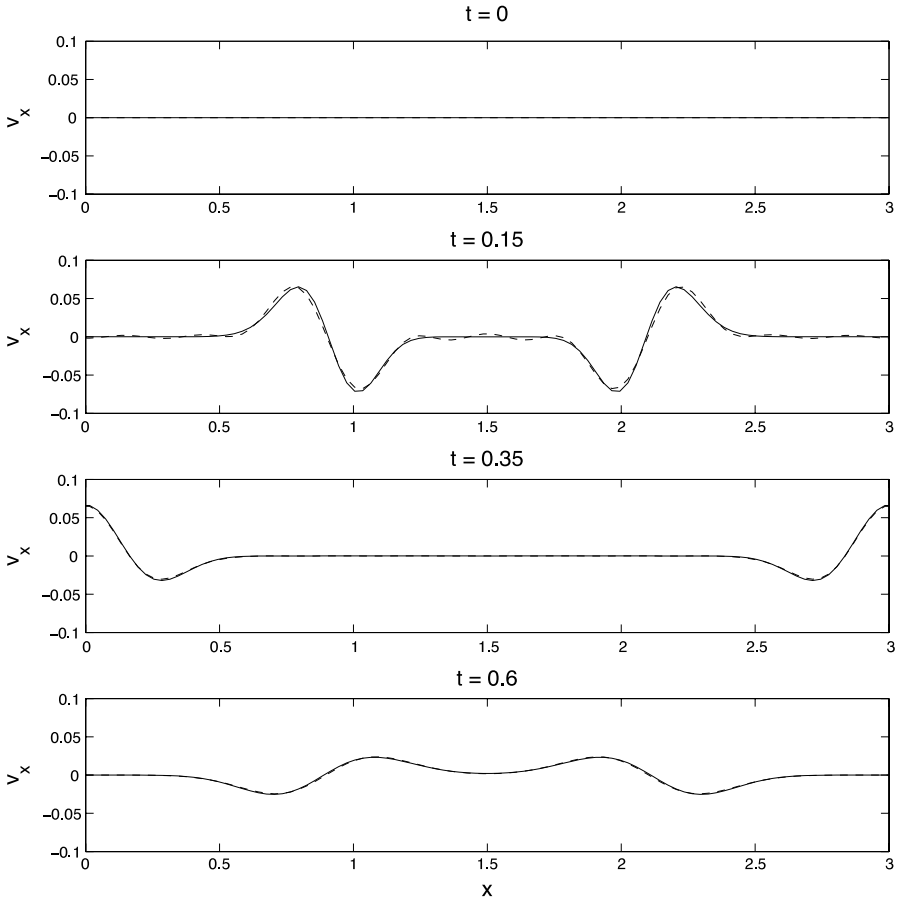

Fig. 5. Profile of velocity v_x in the cross-section $y = L_y/2$ at $t = 0, 0.15, 0.35, 0.6$. The solid line corresponds to the numerical solution while the dashed line corresponds to the exact solution.

where κ is a real constant. This leads to solving the boundary value problem

$$\begin{aligned} &X'' + \kappa X = 0, \\ &X'(0) = X'(L) = 0, \end{aligned} \tag{B.4}$$

by virtue of (B.2), together with the initial value problem

$$\begin{aligned} &T'' + \kappa \left(\frac{\lambda^{(1)} + 2\mu^{(1)}}{\rho^{(s)}} T + \frac{\lambda^{(2)} + 2\mu^{(2)}}{\rho^{(s)}} T' \right) = 0, \\ &T'(0) = 0, \end{aligned} \tag{B.5}$$

by virtue of (B.3).

To solve (B.4), we consider three cases:

1. $\kappa = 0$ implies $X(x) = Ax + B$ and thus
$$X(x) = B = \text{constant},$$
according to the boundary conditions.
2. $\kappa < 0$ implies
$$X(x) = A\cosh(\sqrt{-\kappa}x) + B\sinh(\sqrt{-\kappa}x),$$
but $A = B = 0$ according to the boundary conditions.
3. $\kappa > 0$ implies
$$X(x) = A\cos(\sqrt{\kappa}x) + B\sin(\sqrt{\kappa}x),$$

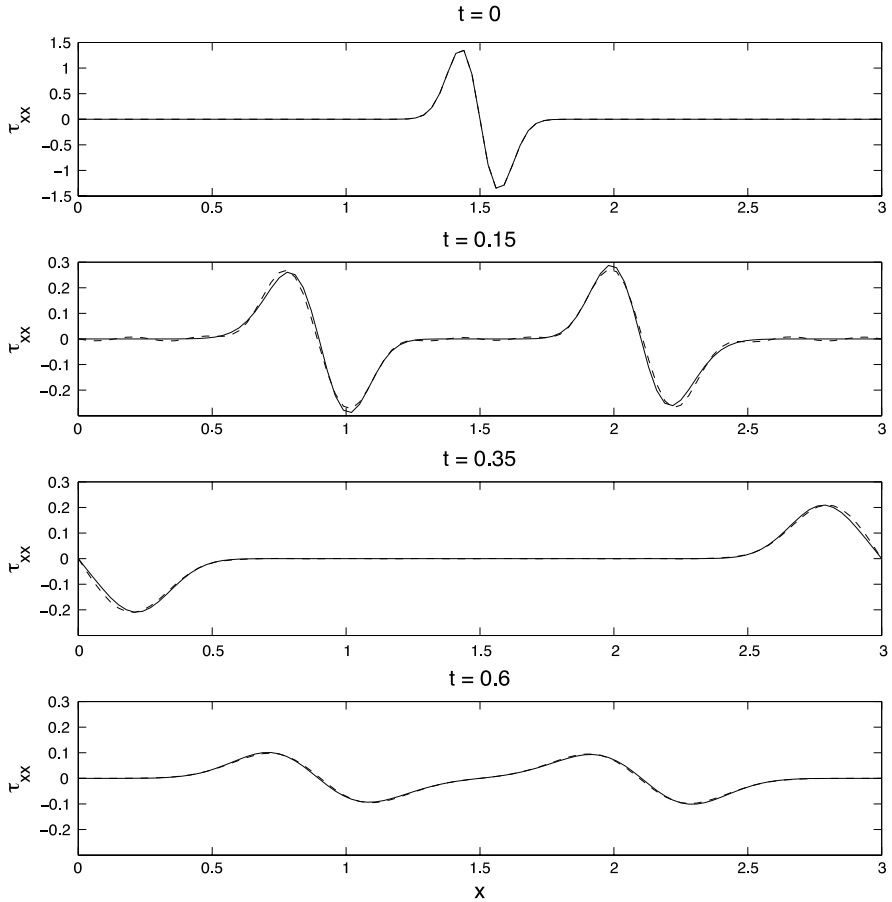

Fig. 6. Profile of stress τ_{xx} in the cross-section $y = L_y/2$ at $t = 0, 0.15, 0.35, 0.6$. The solid line corresponds to the numerical solution while the dashed line corresponds to the exact solution.

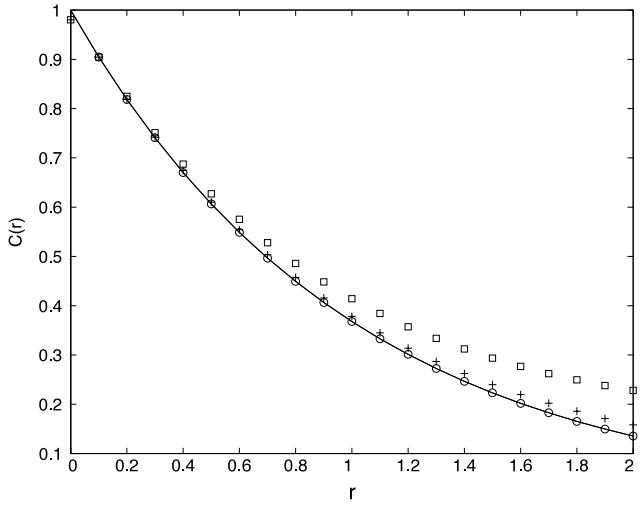

Fig. 7. Exponential covariance function $C(r)$ of the two-dimensional random field. The solid line represents the theoretical covariance. The simulated covariances correspond to $L = 4$ (squares), 8 (crosses) and 16 (circles).

where $B = 0$ and

$$\kappa = \left(\frac{n\pi}{L_x}\right)^2, \quad n \in \mathbb{N}^+, \tag{B.6}$$

so that there are non-trivial solutions, according to the boundary conditions.

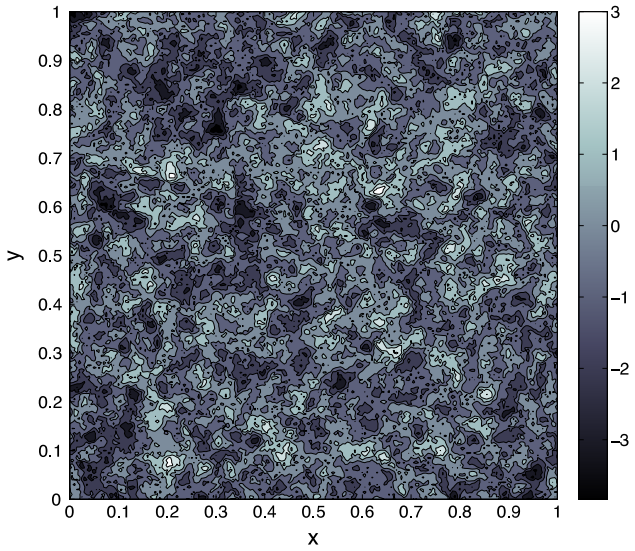

Fig. 8. Simulated two-dimensional random field $z(\mathbf{x})$ for an exponential covariance function with $L = 16$.

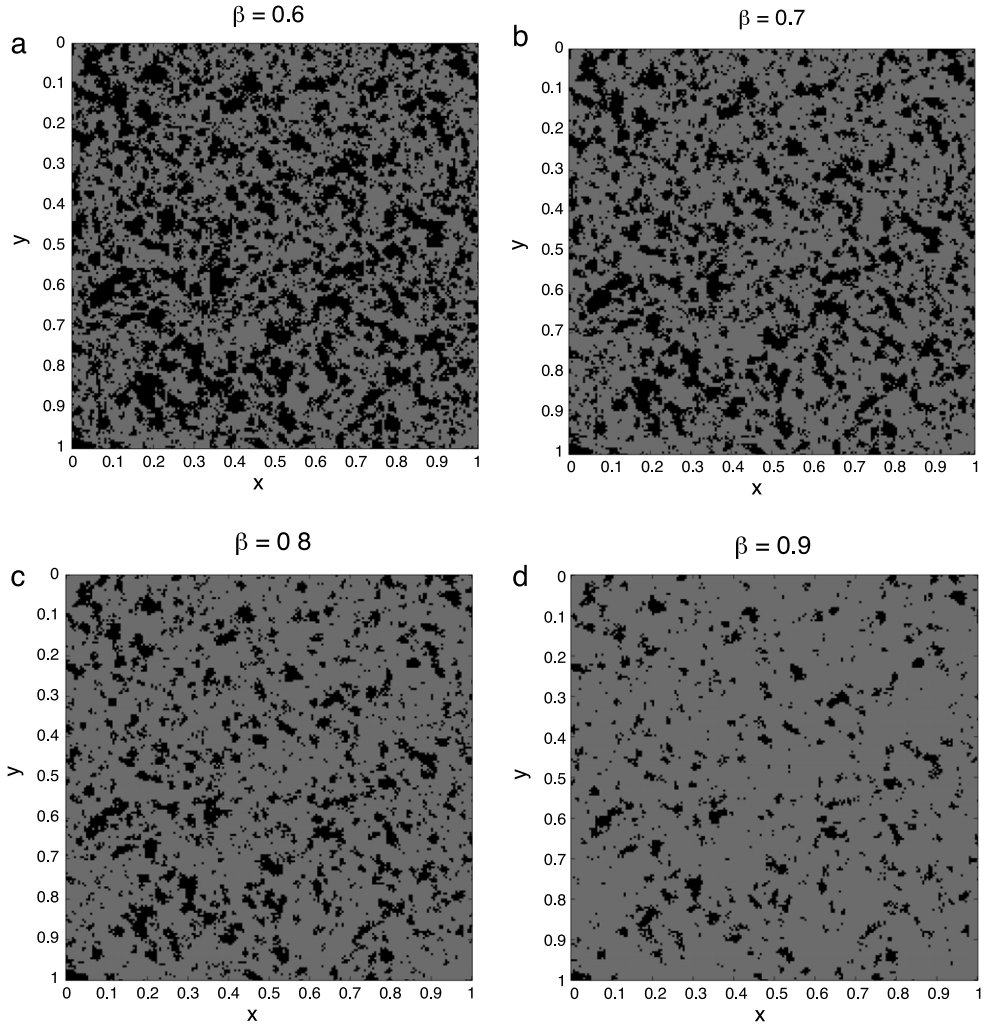

Fig. 9. Random spatial distributions of fluid and solid points for $\beta = 0.6, 0.7, 0.8$ and 0.9, generated from the two-dimensional field in Fig. 8. The black area is solid while the gray area is fluid.

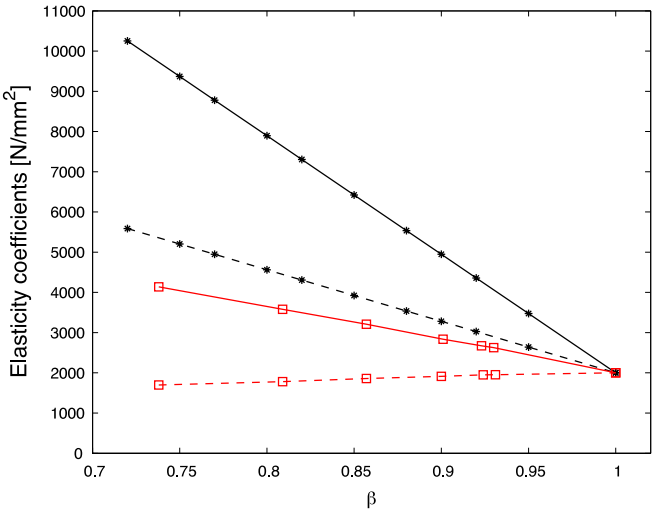

Fig. 10. Elasticity coefficients C_{11} (solid line) and C_{12} (dashed line) vs. porosity β. Our numerical results are in black (stars) while those of Ilic et al. [34] are in red (squares).

Therefore (B.4) admits an infinite number of solutions in the form

$$X_n(x) = A_n \cos\left(\frac{n\pi x}{L_x}\right), \quad n \in \mathbb{N}. \tag{B.7}$$

Then substituting (B.6) (for $n \in \mathbb{N}$) into (B.5), we obtain

$$T'' + C_n T' + D_n T = 0, \tag{B.8}$$

where

$$C_n = \frac{(\lambda^{(1)} + 2\mu^{(1)})n^2\pi^2}{\rho^{(s)}L_x^2}, \qquad D_n = \frac{(\lambda^{(2)} + 2\mu^{(2)})n^2\pi^2}{\rho^{(s)}L_x^2}.$$

Solutions to (B.8) are of the form

$$T_n(t) = a_n e^{-(C_n - \sqrt{C_n^2 - 4D_n})t/2} + b_n e^{-(C_n + \sqrt{C_n^2 - 4D_n})t/2}, \tag{B.9}$$

with

$$a_n = \frac{\sqrt{C_n^2 - 4D_n} + C_n}{\sqrt{C_n^2 - 4D_n} - C_n}\, b_n, \tag{B.10}$$

according to the initial condition $T'(0) = 0$.

By the superposition principle, the general solution of (B.1)–(B.3) can be written as

$$u_x(x, t) = a_0 + \sum_{n=1}^{\infty}\left[a_n e^{-\left(C_n - \sqrt{C_n^2 - 4D_n}\right)t/2} + b_n e^{-\left(C_n + \sqrt{C_n^2 - 4D_n}\right)t/2}\right]\cos\left(\frac{n\pi x}{L_x}\right).$$

Using the remaining initial condition $u(x, 0) = f(x)$, we have

$$u_x(x, 0) = a_0 + \sum_{n=1}^{\infty}(a_n + b_n)\cos\left(\frac{n\pi x}{L_x}\right) = f(x),$$

which is a Fourier cosine series for $f(x)$. Accordingly, the Fourier coefficients are defined by

$$a_0 = \frac{1}{L_x}\int_0^{L_x} f(x)\, dx,$$

$$a_n + b_n = \frac{2}{L_x}\int_0^{L_x} f(x)\cos\left(\frac{n\pi x}{L_x}\right) dx.$$

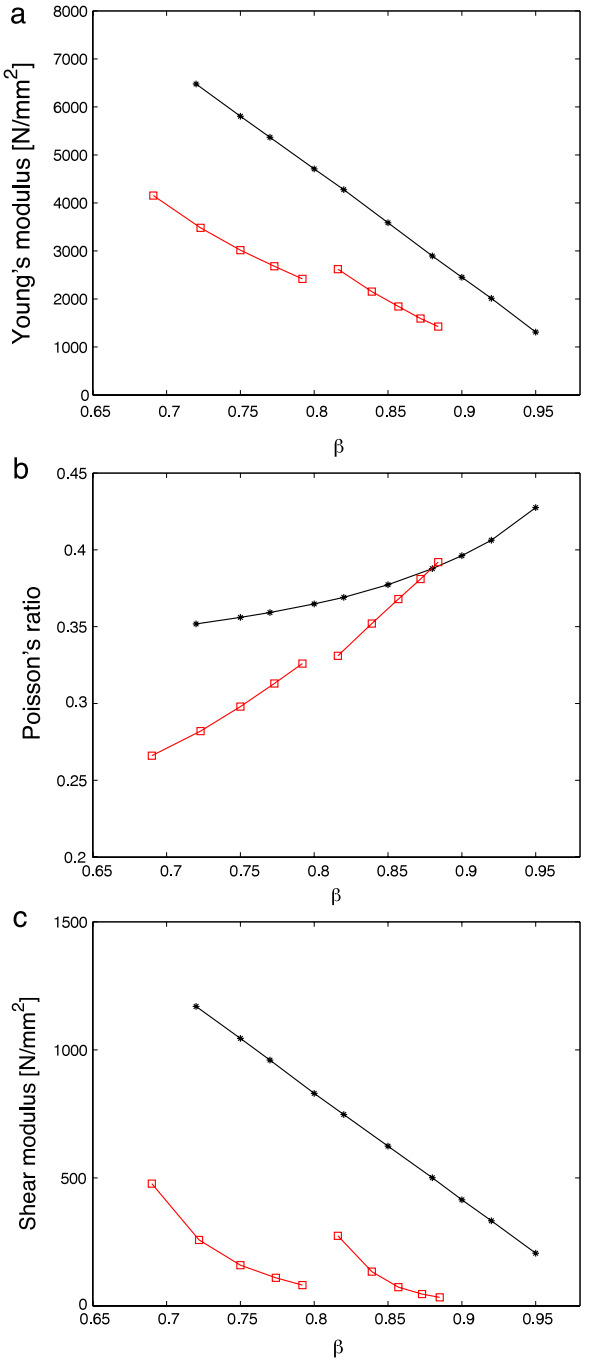

Fig. 11. Effective material parameters: (a) Young's modulus E, (b) Poisson's ratio ν and (c) shear modulus G vs. porosity β. Our numerical results are in black (stars) while those of Ilic et al. [34] are in red (squares).

Recalling the relation (B.10) between a_n and b_n, we finally find

$$a_n = \frac{\sqrt{C_n^2 - 4D_n} + C_n}{L_x\sqrt{C_n^2 - 4D_n}} \int_0^{L_x} f(x) \cos\left(\frac{n\pi x}{L_x}\right) dx,$$

$$b_n = \frac{\sqrt{C_n^2 - 4D_n} - C_n}{L_x\sqrt{C_n^2 - 4D_n}} \int_0^{L_x} f(x) \cos\left(\frac{n\pi x}{L_x}\right) dx.$$

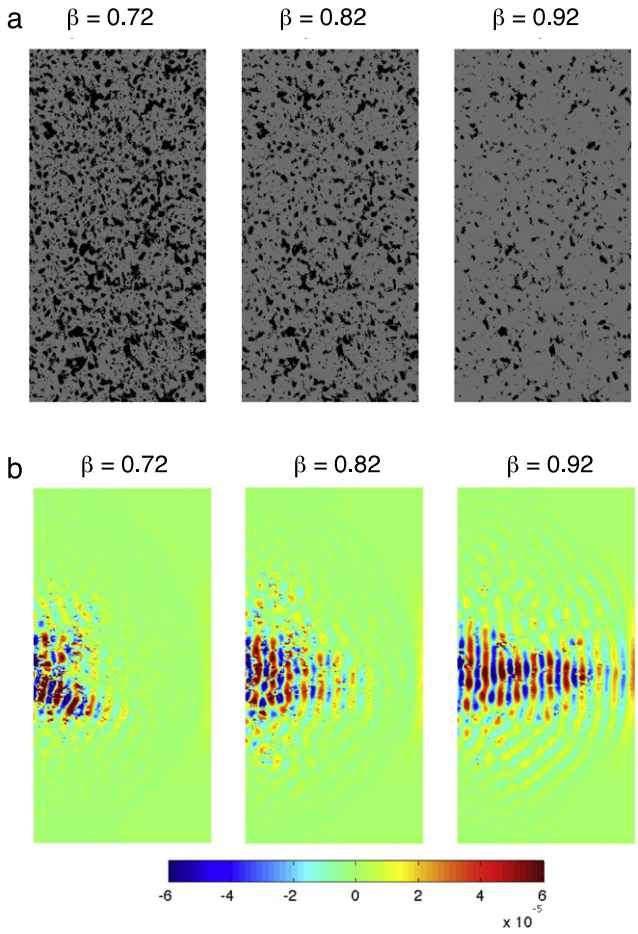

Fig. 12. (a) Random spatial distributions of fluid–solid points for $\beta = 0.72, 0.82, 0.92$. (b) Two-dimensional color plot of displacement u_x at $t = 1$ for $f_c = 1.1$ MHz and $\beta = 0.72, 0.82, 0.92$ in the absence of viscosity. The values of u_x are magnified by a factor of 10^3.

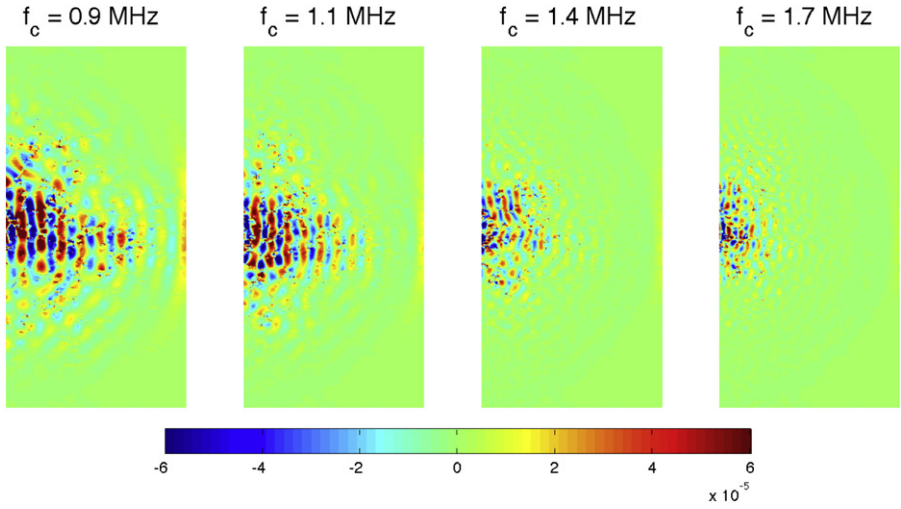

Fig. 13. Two-dimensional color plot of displacement u_x at $t = 1$ for $\beta = 0.82$ and $f_c = 0.9, 1.1, 1.4, 1.7$ MHz in the absence of viscosity. The values of u_x are magnified by a factor of 10^3.

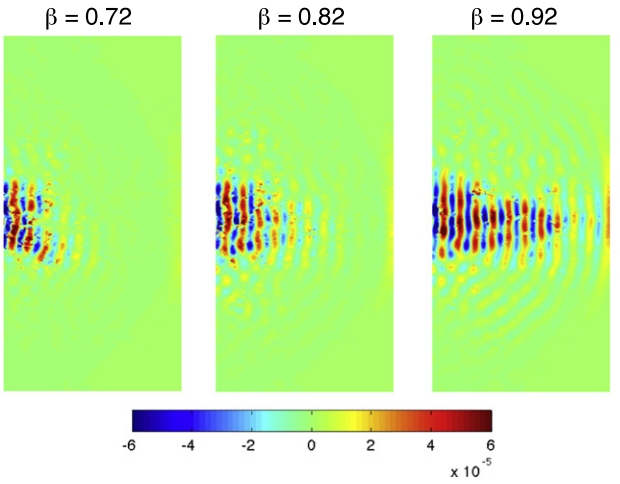

Fig. 14. Two-dimensional color plot of displacement u_x at $t = 1$ for $f_c = 1.1$ MHz and $\beta = 0.72, 0.82, 0.92$ with viscosity. The values of u_x are magnified by a factor of 10^3.

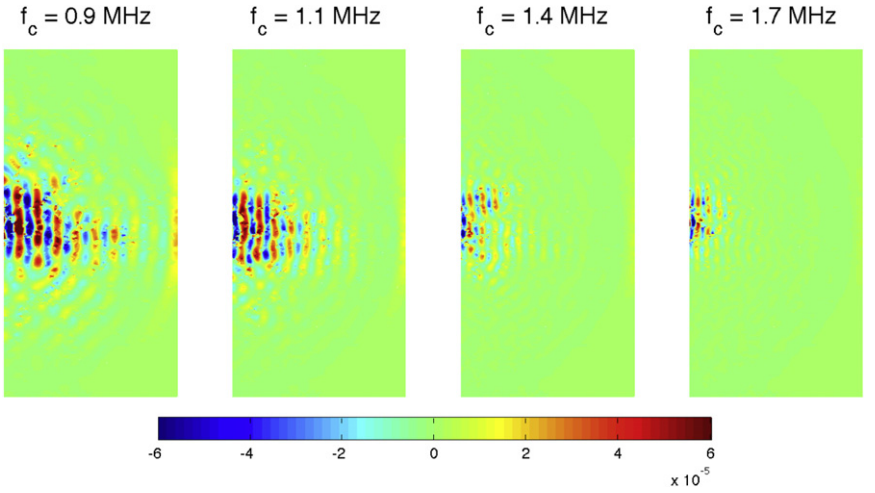

Fig. 15. Two-dimensional color plot of displacement u_x at $t = 1$ for $\beta = 0.82$ and $f_c = 0.9, 1.1, 1.4, 1.7$ MHz with viscosity. The values of u_x are magnified by a factor of 10^3.

References

[1] R. Ashman, J. Corin, C. Turner, Elastic properties of cancellous bone: measurement by an ultrasonic technique, J. Biomech. 20 (1987) 979–986.
[2] R. Ashman, J. Rho, Elastic modulus of trabecular bone material, J. Biomech. 21 (1988) 177–181.
[3] E. Bossy, M. Talmant, P. Laugier, 2d simulation of the axial transmission technique on a cortical bone plate, Acoust. Imaging 26 (2002) 69–76.
[4] E. Bossy, M. Talmant, P. Laugier, Effect of bone cortical thickness on velocity measurements using ultrasonic axial transmission: a 2d simulation study, J. Acoust. Soc. Am. 112 (2002) 297–307.
[5] J. Buchanan, R. Gilbert, Measuring osteoporosis using ultrasound, Adv. Scattering and Biomed. Eng. (2004) 484–494.
[6] J. Buchanan, R. Gilbert, K. Khashanah, Determination of the parameters of cancellous bone using low frequency acoustic measurements, J. Comput. Acoust. 12 (2004) 99–126.
[7] J. Buchanan, R. Gilbert, Determination of the parameters of cancellous bone using high frequency acoustic measurements, Math. Comput. Modelling 45 (2007) 281–308.
[8] J. Buchanan, R. Gilbert, Determination of the parameters of cancellous bone using high frequency acoustic measurements ii: inverse problems, J. Comput. Acoust. 15 (2007) 199–220.
[9] S. Chaffai, G. Berger, P. Laugier, Frequency variation of ultrasonic attenuation coefficient of cancellous bone between 0.2 and 2.0 MHz, in: Ultrasonics Symposium, 1998, Proceedings, 1998 IEEE, Vol. 2, IEEE, pp. 1397–1400.
[10] S. Chaffai, V. Roberjot, F. Peyrin, G. Berger, P. Laugier, Frequency dependence of ultrasonic backscattering in cancellous bone: autocorrelation model and experimental results, J. Acoust. Soc. Am. 108 (2000) 2403–2411.
[11] P. Droin, P. Laugier, G. Berger, Ultrasonic attenuation and dispersion of cancellous bone in the frequency range 200–600 kHz, Acoust. Imaging 23 (1997) 157–162.
[12] P. Droin, G. Berger, P. Laugier, Velocity dispersion of acoustic waves in cancellous bone, IEEE Trans. Ultrason. Ferroelectr. Freq. Control 45 (1998) 581–592.
[13] Z. Fellah, J. Chapelon, S. Berger, W. Lauriks, C. Depollier, Ultrasonic wave propagation in human cancellous bone: application of biot theory, J. Acoust. Soc. Am. 116 (2004) 61–73.

[14] M. Fellah, Z. Fellah, F. Mitri, E. Ogam, C. Depollier, Transient ultrasound propagation in porous media using biot theory and fractional calculus: application to human cancellous bone, J. Acoust. Soc. Am. 133 (2013) 1867–1881.
[15] T. Haire, C. Langton, Biot theory: a review of its application to ultrasound propagation through cancellous bone, Bone 24 (1999) 291–295.
[16] M. Hobatho, J. Rho, R. Ashman, Atlas of mechanical properties of human cortical and cancellous bone, J. Biomech. 25 (1992) 669.
[17] A. Hosokawa, T. Otani, Ultrasonic wave propagation in bovine cancellous bone, J. Acoust. Soc. Am. 101 (1997) 1219.
[18] M. Kaczmarek, M. Pakuła, J. Kubik, Multiphase nature and structure of biomaterials studied by ultrasounds, Ultrasonics 38 (2000) 703–707.
[19] T. Kundu, Ultrasonic Nondestructive Evaluation: Engineering and Biological Material Characterization, CRC Press, 2004.
[20] R. Lakes, H. Yoon, J. Katz, et al., Slow compressional wave propagation in wet human and bovine cortical bone, Science 220 (1983) 513–515.
[21] C. Langton, C. Njeh, The physical measurement of bone, in: Series in Medical Physics and Biomedical Engineering, Taylor & Francis, 2003.
[22] C. Langton, S. Palmer, R. Porter, The measurement of broadband ultrasonic attenuation in cancellous bone, Eng. Med. 13 (1984) 89–91.
[23] M. McKelvie, S. Palmer, The interaction of ultrasound with cancellous bone, Phys. Med. Biol. 36 (2000) 1331–1340.
[24] C. Njeh, Quantitative Ultrasound: Assessment of Osteoporosis and Bone Status, Martin Dunitz, 1999.
[25] R. Othman, G. Gary, Dispersion identification using the fourier analysis of resonances in elastic and viscoelastic rods, in: Acoustics, Mechanics, and the Related Topics of Mathematical Analysis: CAES Du CNRS, Frejus, France, 18–22 June 2002, p. 229.
[26] F. Padilla, F. Peyrin, P. Laugier, Prediction of backscatter coefficient in trabecular bones using a numerical model of three-dimensional microstructure, J. Acoust. Soc. Am. 113 (2003) 1122–1129.
[27] J. Rho, An ultrasonic method for measuring the elastic properties of human tibial cortical and cancellous bone, Ultrasonics 34 (1996) 777–783.
[28] R. Strelitzki, J. Evans, On the measurement of the velocity of ultrasound in the os calcis using short pulses, European J. Ultrasound 4 (1996) 205–213.
[29] K. Wear, Frequency dependence of ultrasonic backscatter from human trabecular bone: theory and experiment, J. Acoust. Soc. Am. 106 (1999) 3659–3664.
[30] K. Wear, Ultrasonic attenuation in human calcaneus from 0.2 to 1.7 MHz, IEEE Trans. Ultrason. Ferroelectr. Freq. Control 48 (2001) 602–608.
[31] K. Wear, Fundamental precision limitations for measurements of frequency dependence of backscatter: applications in tissue-mimicking phantoms and trabecular bone, J. Acoust. Soc. Am. 110 (2001) 3275–3282.
[32] J. Williams, Ultrasonic wave propagation in cancellous and cortical bone: prediction of some experimental results by Biot's theory, J. Acoust. Soc. Am. 91 (1992) 1106–1112.
[33] C. Langton, C. Njeh, R. Hodgskinson, J. Currey, Prediction of mechanical properties of the human calcaneus by broadband ultrasonic attenuation, Bone 18 (1996) 495–503.
[34] S. Ilic, K. Hackl, R. Gilbert, Application of the multiscale fem to the modeling of cancellous bone, Biomech. Model. Mechanobiol. 9 (2010) 87–102.
[35] E. Bossy, F. Padilla, F. Peyrin, P. Laugier, Three-dimensional simulation of ultrasound propagation through trabecular bone structures measured by synchrotron microtomography, Phys. Med. Biol. 50 (2005) 5545–5556.
[36] A. Hosokawa, Development of a numerical cancellous bone model for finite-difference time-domain simulations of ultrasound propagation, IEEE Trans. Ultrason. Ferroelectr. Freq. Control 55 (2008) 558–562.
[37] J.L. Buchanan, R.P. Gilbert, M. jung, Y. Ou, Wavelet decomposition of transmitted ultrasound wave through a 1-d muscle-bone system, J. Biomech. 44 (2011) 352–358.
[38] J. Buchanan, R. Gilbert, M. Ou, Recovery of the parameters of cancellous bone by inversion of effective velocities, and transmission and reflection coefficients, Inverse Problems 27 (2011) 125006.
[39] R. Graves, Simulating seismic wave propagation in 3d elastic media using staggered-grid finite differences, Bull. Seismol. Soc. Amer. 86 (1996) 1091–1106.
[40] R. Gilbert, P. Guyenne, J. Li, Simulation of a mixture model for ultrasound propagation through cancellous bone using staggered-grid finite differences, J. Comput. Acoust. 21 (2013) 1–28.
[41] R. Lakes, H. Yoon, J. Katz, Ultrasonic wave propagation and attenuation in wet bone, J. Biomed. Eng. 8 (1986) 143–148.
[42] S. Chaffai, F. Padilla, G. Berger, P. Laugier, In vitro measurement of the frequency-dependent attenuation in cancellous bone between 0.2 and 2 MHz, J. Acoust. Soc. Am. 108 (2000) 1281–1289.
[43] A. Mantoglou, J. Wilson, The turning bands method for simulation of random fields using line generation by a spectral method, Water Resour. Res. 18 (1982) 1379–1394.
[44] A. Tompson, R. Ababou, L. Gelhar, Implementation of the three-dimensional turning bands random field generator, Water Resour. Res. 25 (1989) 2227–2243.
[45] M. Shinozuka, C.-M. Jan, Digital simulation of random processes and its applications, J. Sound Vib. 25 (1972) 111–128.
[46] B. Auld, Acoustic Fields and Waves in Solids, Vol. 1, Wiley, 1973.
[47] D. Royer, E. Dieulesaint, D. Morgan, Elastic Waves in Solids I: Free and Guided Propagation, in: Advanced Texts in Physics, Springer, 2000.
[48] M. Sasso, G. Haiat, Y. Yamato, S. Naili, M. Matsukawa, Frequency dependence of ultrasonic attenuation in bovine cortical bone: an in vitro study, Ultrasound Med. Biol. 33 (2007) 1933–1942.
[49] B. Garcia, R. Cobbold, F. Foster, K. McNeill, Ultrasonic attenuation in bone, in: 1978 Ultrasonics Symposium, IEEE, pp. 327–330.
[50] S. Goss, R. Johnston, F. Dunn, et al., Comprehensive compilation of empirical ultrasonic properties of mammalian tissues, J. Acoust. Soc. Am. 64 (1978) 423–457.